Optothermally Responsive Nanocomposite Generating Mechanical Forces for Cells Enabled by Few-Walled Carbon Nanotubes

Yuze Zeng and Jennifer Q. Lu*

School of Engineering, University of California-Merced, Merced, California 95343, United States

ABSTRACT We have designed and fabricated a nanocomposite substrate that can deliver spatially and temporally defined mechanical forces onto cells. This nanocomposite substrate comprises a 1.5-mm-thick near-infrared (NIR) mechanoresponsive bottom layer of few-walled carbon nanotubes (FWCNTs) that are uniformly distributed and covalently connected to thermally responsive poly(*N*-isopropylacrylamide) and an approximately 0.15-mm-thick cell-seeding top layer of collagen-functionalized poly(acrylic acid)-*co*-poly(*N*-isopropylacrylamide) that interpenetrates into the bottom layer. Covalent coupling of all the components and uniform distribution of FWCNTs lead to a large local mechanoresponse. As an example, 50% change in strain at the point of irradiation on the order of 0.05 Hz can be produced reversibly under NIR stimulation with 0.02 wt % FWCNTs. We have further demonstrated that the mechanical strain imposed by NIR stimulation can be transmitted onto cells. Human fetal hepatocytes change shape with no sign of detrimental effect on cell viability. To the best of our knowledge, this is the first demonstration of a nanocomposite platform that can generate fast and controlled mechanical force to actuate cells. Since the amplitude, location, and timing of force can be controlled remotely with NIR, the nanocomposite substrate offers the potential to provide accurately designed force sequences for tissue engineering.

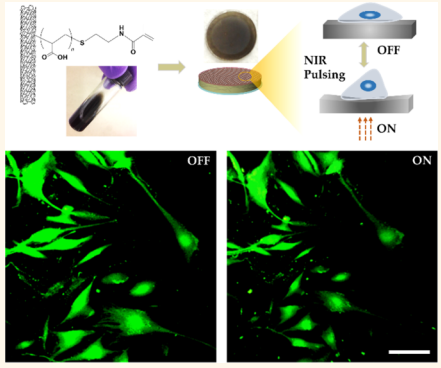

KEYWORDS: macromonomer-grafted few-walled carbon nanotubes · PNIPAM · nanocomposites · optothermal effect · remote near-infrared actuation · spatiotemporal controlled forces

There is accumulating evidence that mechanical forces play essential roles in tissue embryogenesis, somitogenesis, and organogenesis.[1−6] One oft-quoted example is that dynamic shear stress leads to the formation of a highly branched hierarchical vascular tree.[7] As cells mature, biophysical forces remain critical in tissue maintenance and repair.[8]

Significant progress has been made toward understanding mechanotransduction. A small modification of physical forces, *i.e.*, type, amplitude, and frequency of forces, can result in alteration of cell fate and function that far exceeds previous expectations.[9−14] For example, external mechanical tension applied to cardiac tissue culture can induce rapid formation of interconnected, longitudinally oriented cardiac muscle bundles with morphological features resembling those of adult native tissue.[9] Constant perfusion has been found to generate engineered bones with comparable composition/properties to native ones.[11] It has been recognized that spatially and temporally well-defined mechanical force is critical for cell function.[15] This is highlighted by the recent demonstration that imposing a sequence of mechanical cues at an appropriate time interval can coax a single stem cell to differentiate into an organized germ layer.[16] Unfortunately, most existing force-generating systems produce only a single force format across the entire cell-seeding substrate.

Abrupt strain changes during phase transitions such as the melting of poly(ε-caprolactone)[17] and the swelling/deswelling of poly(*N*-isopropylacrylamide) (PNIPAM) when the temperature fluctuates around its lower critical solution temperature (LCST)[18−20] have been exploited to produce mechanical forces *via* strain/deformation. A thermally driven phase transition is often difficult to

* Address correspondence to jlu5@ucmerced.edu.

Received for review September 6, 2014 and accepted October 19, 2014.

Published online October 19, 2014
10.1021/nn505042b

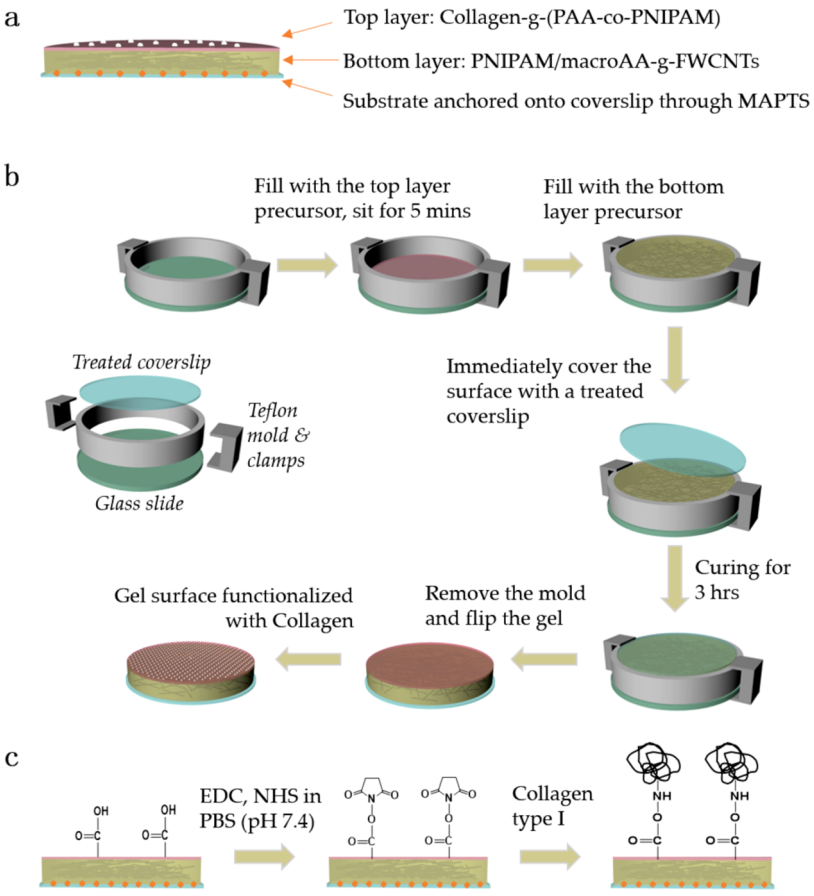

Figure 1. (a) Conceptual drawing of the bilayer nanocomposite substrate. (b) Schematic process flow of the formation of the bilayer nanocomposite substrate. (c) Chemical reaction scheme to graft collagen onto the top layer of a nanocomposite substrate.

confine to a localized region without involving complex fabrication steps to embed resistor-based microheaters.[21] Moreover, polymers subjected to repeated mechanical loading are likely to undergo irreversible microstructural changes.[22,23]

Carbon nanotubes (CNTs) have been employed extensively to create multifunctional polymeric hydrogel-nanocomposites for tissue engineering.[24−28] In particular, CNTs have been used to enhance the resilience of polymeric hydrogels to mechanical loads and to extend material lifetime.[28−30] Due to their excellent near-infrared (NIR) absorption properties, CNTs have also been employed as nanoheaters to generate localized heating.[24,31−33] Few-walled CNTs (FWCNTs) can absorb NIR light strongly, serving as nanoheaters that convert NIR photon energy into localized heat. Without FWCNTs the pure PNIPAM hydrogel will not absorb NIR light and thus will not be heated up. The advantages of using FWCNTs are that (i) they are small, if compared with multiwalled CNTs, thus can be more readily dispersed; (ii) differing from single-walled CNTs, whose mechanical properties can be degraded by the surface functionalization, the outer wall of FWCNTs can be functionalized with macromonomers, which in turn are copolymerized with NIPAM to covalently connect these two dissimilar materials (*i.e.*, CNTs and the responsive polymer) to form a true composite; and (iii) the presence of a highly dispersed and small amount of covalently bound FWCNTs has been shown to be able to effectively heat the hydrogel and have no detrimental effect on swelling and deswelling kinetics. As a result, greatly enhanced mechanical properties were observed with only 0.02 wt % CNTs. We have designed and fabricated a bilayer nanocomposite substrate that can apply spatiotemporal force patterns to seeded cells. Figure 1 includes conceptual drawings of the substrate and its formation process. The substrate is made of a 1.5-mm-thick bottom layer of NIR mechanoresponsive nanocomposite and an approximately 0.15-mm-thick cell-seeding top layer that is intercalated and covalently bound to the bottom layer. The bottom layer consists of FWCNTs, uniformly populated and covalently linked to the thermally responsive PNIPAM matrix. Mechanical strain resulting from heating the PNIPAM above its LCST can be produced remotely *via* NIR irradiation. Due to the highly spatial and temporal variability of photostimulation sources, well-defined and engineered force patterns can be created by patterned irradiation. Since healthy cells and tissues have little absorption in the

NIR region, NIR is safer when compared with UV or visible sources.[34,35] We have designed a macromonomer that is grafted onto FWCNTs for the formation of a nanocomposite in which FWCNTs are evenly distributed. We have demonstrated that with 0.02 wt % FWCNTs in the bottom layer, this bilayer nanocomposite can generate reversible local actuation as large as 50% strain at the point of irradiation and 30% strain in the adjacent area at physiologically relevant temperatures.

We have further demonstrated that the shapes of cells, human telomerase reverse transcriptase-reconstituted human fetal hepatocytes (hTERT-FHs), can be changed under NIR stimulation. Since the top layer is interspersed into the bottom layer with a thickness of one tenth of the bottom layer, forces generated in the bottom layer nanocomposite are successfully transmitted onto cells that adhere to the top layer. Because the extracellular proteins, collagens,[36] are covalently attached to the top surface, cells remain on the substrate during actuation. The result implies that both the bilayer nanocomposite and the amount of NIR influx used for actuation do not cause appreciable cell apoptosis. It is known that achieving functional hepatic differentiation through chemical induction remains challenging.[37] Engineering mechanical stimulation can provide an opportunity to achieve functional liver cells.

RESULTS AND DISCUSSION

Synthesis and Characterizations of the NIR Mechanoresponsive Bottom Layer. To provide uniform and controlled strain/deformation, it is essential to populate CNTs evenly throughout the entire layer. We used few-walled CNTs as nanoheaters with the following considerations. Unlike single-walled CNTs, they typically have 2−5 walls. The outer layer can be consumed for surface functionalization, while the inner walls remain intact. Therefore, their outstanding mechanical properties as well as NIR absorption efficacy can be preserved.[38−40] Differing from multiwalled CNTs that have more than 10 walls, they can be dispersed more readily. Since CNTs act as barriers to prevent the propagation of strain/deformation, too high a concentration of CNTs will result in damping of the mechanoresponse. It is thus important to have CNTs that are covalently linked to the hydrogel matrix so that no CNTs will be extruded out during repeated actuation. For effective reinforcement purposes, a strong interface between the CNTs and polymer is also required.

To attain a nanocomposite with minimum amount of evenly distributed, covalently bound CNTs in the hydrogel matrix, we modified the previously published method that was developed by us to graft polymer with controlled molecular weight onto CNTs,[41,42] for the synthesis of acrylic acid macromonomers-grafted few-walled CNTs (macroAA-*g*-FWCNTs). The synthetic procedure is depicted in Figure 2a. MacroAA-*g*-FWCNTs, in turn, were copolymerized with NIPAM to form a nanocomposite that serves as the bottom layer.

Acetone, a poor solvent for poly(acrylic acid) (PAA), was employed to graft low molecular weight PAA onto FWCNTs. To form macroAA-*g*-FWCNTs, an amino-mercaptan chain transfer agent and subsequent reaction with methacryloyl chloride were used to provide each PAA chain with a polymerizable terminal

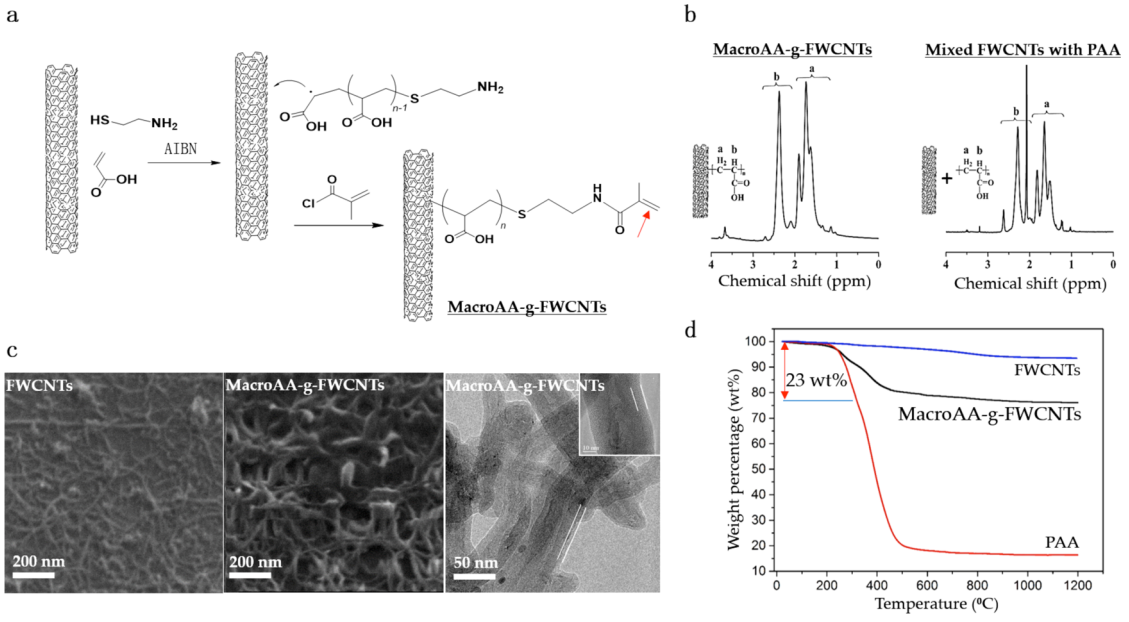

Figure 2. (a) Synthetic scheme for generating macroAA-*g*-FWCNTs with a terminal methacrylamidyl group. (b) ^{1}H NMR comparison between macroAA-*g*-FWCNTs and a mixture of PAA and FWCNTs. (c) Scanning electron microscopic image of pure FWCNTs and scanning electron microscopic image and transmission electron microscopic image of macroAA-*g*-FWCNTs. (d) Thermogravimetric analysis of PAA only, FWCNTs, and macroAA-*g*-FWCNTs in N_2 (10 °C/min); double arrow demarcates the weight loss due to macroAA decomposition.

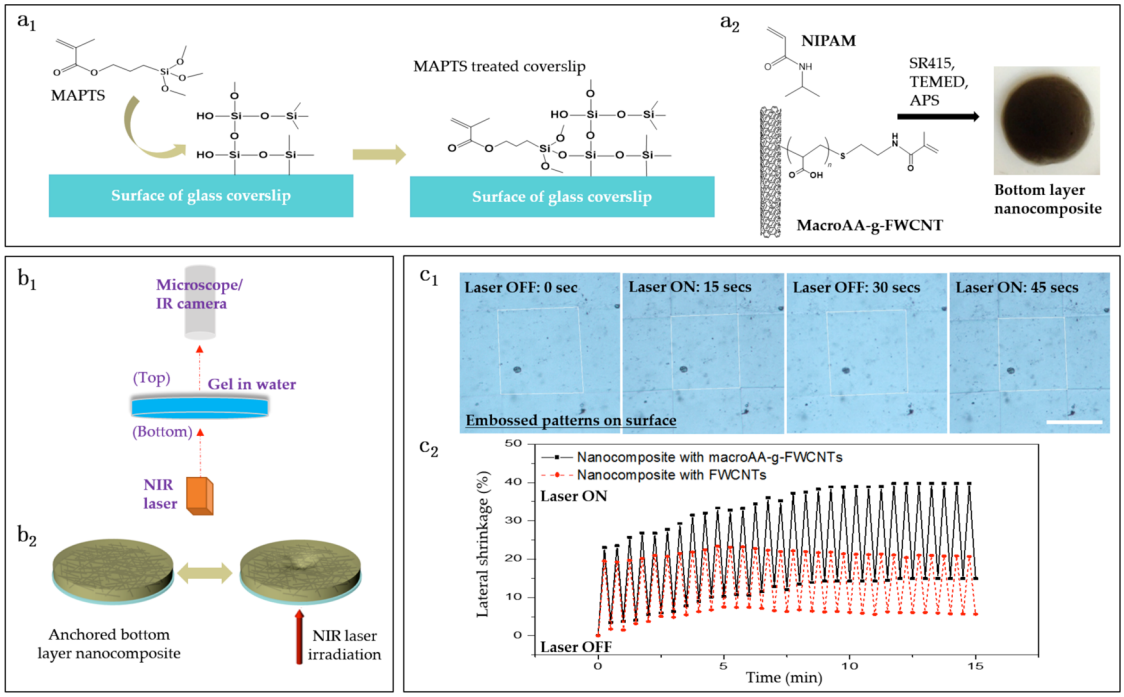

Figure 3. (a) Schematic drawings show the activation of a glass coverslip (a_1) and the formation of a bottom layer nanocomposite (a_2). (b) Cartoons demonstrate the setup for studying the nanocomposite optothermal response (b_1) and the reversible shrinkage of the bottom layer nanocomposite upon NIR pulsing (b_2). (c) Lateral shrinkage produced by the cyclic NIR irradiation (980 nm, 200 mW, 0.033 Hz), calculated from the square area (delineated in white) of the optical images of the patterned surface (c_1). Scale bar: 100 μm. Black curve is the nanocomposite generated with macroAA-*g*-FWCNTs; red curve is the nanocomposite generated with pure FWCNTs (c_2).

methacrylamidyl group. Sonication in deionized water followed by filtration was used to remove ungrafted FWCNTs. The ^{1}H NMR analysis in Figure 2b shows that the bands associated with methylene groups are broadened as a result of grafting when compared with a mixture of PAA and FWCNTs. The scanning electron microscopic images in Figure 2c show a smooth layer coated on CNT surfaces. This is indicative that a thin polymer layer was grafted on CNTs. The thickness of the grafted polymer layer is around 12 nm based on the transmission electron microscopic image analysis, shown in the same figure. According to the thermogravimetric analysis displayed in Figure 2d, grafted macroAA degrades at higher temperature if compared with pure PAA. This is another piece of evidence supporting that about 23 wt % macroAA using acetone as a solvent has been grafted through the precipitation polymerization.

The precursor solution for the bottom layer comprises 0.025 wt % macroAA-*g*-FWCNTs, which is equivalent to 0.02 wt % FWCNTs, NIPAM, a triacrylate polyethylene glycol cross-linker (SR415), ammonium persulfate (APS) initiator, and an accelerator, *N*,*N*,*N*′,*N*′-tetramethylethylenediamine (TEMED). To achieve controlled deformation under NIR illumination while maintaining a flat surface for high-resolution optical imaging and for effective cell actuation, 3-(trimethoxysilyl)propyl methacrylate (MAPTS) is employed to functionalize the glass coverslip surface with methacryloyl groups, as illustrated in Figure 3a_1. Consequently, covalent linkages between the coverslip and PNIPAM and FWCNTs within the nanocomposite can be established during the polymerization, as illustrated in Figure 3a_2. The average thickness of this nanocomposite is about 1.5 mm. As seen in the optical image shown in the same figure, the nanocomposite displays a uniform shade of gray. This suggests that CNTs are uniformly distributed in the nanocomposite. On the contrary, FWCNTs without macroAA grafting agglomerate into clusters that are visible to the naked eye, as evidenced by optical images shown in Figure S1.

Since CNTs can efficiently convert NIR photon energy to thermal energy, localized heating is expected from a "point" laser source instead of heating the entire substrate and culture solution. Figure 3b_1 is a schematic drawing depicting our experimental setup, while Figure 3b_2 is a set of conceptual drawings illustrating the strain/deformation of this nanocomposite under conditions of localized heating and cooling. To examine the optothermal effect, we imprinted the surface of the nanocomposite with a series of patterns that includes a feature of a 150 μm square, 10 μm in depth, using a silicon mold. When the laser is on, the substrate that is exposed to illumination will be deswollen as a result of the optothermally induced temperature rise above the LCST, as manifested by the lateral shrinkage of the imprinted patterns. During the

NIR pulsing (980 nm, 200 mW, 0.033 Hz), the amount of shrinkage was calculated based on the optical images captured throughout the cyclic actuation and was plotted against time as displayed in Figure 3c. There is a baseline shift in Figure $3c_2$ as internal stress is released during the initial cycles and heat builds up due to the relatively high frequency of NIR pulsing. After extended cycles, a lateral shrinkage close to 40% is observed repeatedly. Due to the relatively large pattern compared to the laser beam, the lateral shrinkage is lower than what we expected. Hence, we used a lower irradiation frequency to let the surface pattern complete each swelling/deswelling cycle, where a 50% lateral shrinkage was observed, as can be seen in Figure S2. We attribute the observed efficient and reproducible actuation, offered by this nanocomposite, to the combination of effective NIR absorption by the uniformly distributed FWCNTs and covalent linkages between FWCNTs and the PNIPAM matrix. No FWCNTs were secreted out after extended cycling. In contrast, FWCNTs were extruded out after repeated hydrogel swelling and deswelling for the samples consisting only of physical mixtures of FWCNTs and PNIPAM, *i.e.*, without covalent bonding between PNIPAM and CNTs. This results in reduced shrinkage in response to the same dose of NIR irradiation, as can be seen in the plot. Nevertheless, the amount of FWCNTs being secreted out is too small to measure since the total loading in each piece of nanocomposite is merely 0.02 wt % (*ca.* 0.08 mg). Since pure PNIPAM hydrogel is "transparent" to NIR, we did not observe any dimensional change upon NIR pulsing.

The observed appreciable deformation in the region under laser illumination suggests that a loading of 0.02 wt % FWCNTs is sufficient to heat the hydrogel matrix above the LCST, and the presence of a miniscule amount of FWCNTs does not attenuate the hydrogel's mechanoresponsive behavior. Figure S3 is a comparison of the UV−vis transmission at 600 nm of PNIPAM hydrogels with and without CNTs. As expected, the nanocomposite is more opaque in both the swelling and deswelling states. Doping with a small amount of CNTs leads to a more gradual transition.

Formation of Bilayer Nanocomposite Substrate to Improve Cell Adhesion. PNIPAM-based surfaces have been widely explored for cell sheet harvesting in tissue engineering.[35,43,44] A tissue-like cellular monolayer of homo- or hetero-type cells can be harvested from the "smart" PNIPAM surfaces by lowering the cell culture temperature from 37 °C to 25 °C. In contrast, cells need to be anchored on the substrate in order to "sense" NIR-induced actuation. Figure S4 (left) is a fluorescence image of calcein AM-stained hTERT-FHs on the mechanoresponsive bottom layer nanocomposite. Cells survived after a three-day incubation at 37 °C. However, after being stored at 30 °C for no more than 5 min, cells began to detach as the PNIPAM surface turns hydrophilic when the temperature is below the LCST, as evidenced by the rounded cell shapes.

We thus designed a cell-seeding layer. Figure 1c is the schematic process flow for the formation of collagen-grafted PAA-*co*-PNIPAM as the top layer for cell seeding, which is intercalated and covalently bound to the bottom layer nanocomposite. For sufficient force to be transmitted onto cells, it is important to have a very thin top layer that not only offers sufficient cell adhesion but also interpenetrates into the bottom layer so that these two layers can act as one. We adjusted the concentration and amount of the precursor solution so that the final thickness of the top layer is about 0.15 mm. To form a strong interface, the top layer precursor was introduced during the polymerization of the bottom layer. These two layers are interspersed near the interface and connected through covalent linkages *via* copolymerization.

With 1-ethyl-3-(3-dimethylamino)propyl carbodiimide (EDC)/*N*-hydroxysuccinimide (NHS) as coupling agents, carboxylates (−COOH) from PAA and primary amines ($-NH_2$) from collagen form covalent linkages. As a result, collagen is strongly bound to the rest of the nanocomposite substrate and does not detach from the surface during repeated localized deformation caused by pulsed NIR irradiation. Thus, cells can be "anchored" onto the surface[36] and subjected to repeated mechanical strains. To understand the importance of having covalently grafted collagen, we compared the cell adhesion on a surface coated with collagen without using EDC/NHS, *i.e.*, physisorbed collagen, shown in Figure S4 (right), with surfaces coated with covalently grafted collagens, shown in Figure 4a. After 5 min at 30 °C, cells exhibited spherical shapes indicating that the cells were readily detached from the substrate. This suggests that physically attached collagens might have delaminated from the substrates during swelling. Hence physisorbed collagen could not offer enough adhesion for cells during mechanical actuation.

Figure 4a is a set of fluorescence images of calcein AM-stained hTERT-FHs showing the effect of top layer formulation on cell adhesion before and after extended actuation. The top layers were prepared by copolymerization of AA and NIPAM with the molar ratio of 1:0, 1:1, and 1:2, respectively. After being cultured for 3 days, cells were spread out and healthy as shown in Figure 4a (top panel), except for the case of the AA:NIPAM molar ratio of 1:2. To further demonstrate the cellular behavior in response to mechanical deformation induced by NIR, in our future work we will perform immunostaining to visualize any change of focal adhesions in response to force imposed by this nanocomposite in conjunction with NIR. Nevertheless, after sitting for 2 h at 30 °C and experiencing repeated mechanical deformation by pulsed NIR, cells still adhered well to the substrates, with the exception of the one whose top layer has a high content of PNIPAM

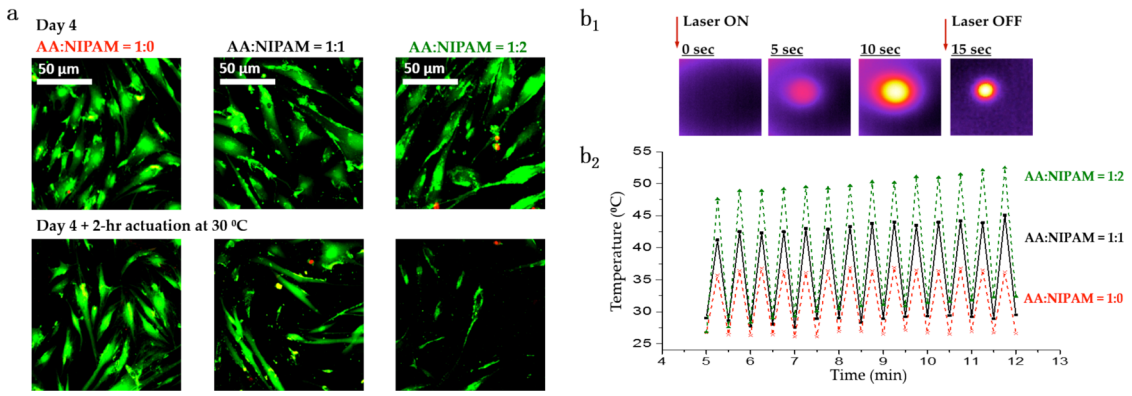

Figure 4. (a) Fluorescence images of calcein AM-stained hTERT-FHs on the bilayer nanocomposite with the collagen-grafted top layer that was prepared using different monomer compositions (AA:NIPAM = 1:0, 1:1, and 1:2). Images were taken before and after a 2 h actuation at 30 °C after incubating for 3 days. (b_1) Thermal images of the bilayer nanocomposite in response to pulsed laser irradiation (980 nm, 200 mW, 0.033 Hz). (b_2) Temperature profiles of the bilayer nanocomposites with the top layer prepared from AA:NIPAM = 1:0, 1:1, and 1:2.

(AA:NIPAM = 1:2). The failure of the 1:2 ratio substrate is due to the combination of an insufficient amount of grafted collagen on the surface, which results from a low concentration of PAA, and a large-volume expansion, which results from a high concentration of PNIPAM swelling below the LCST. Consequently, inadequate cell adhesion and large dimensional change, together with greater hydrophilicity at the swollen state, lead to poor cell adhesion.

Figure 4b_1 contains a set of thermal images taken by an IR camera showing the temperature maps of the top surface of the bilayer nanocomposite substrate during cyclic irradiation. Figure 4b_2 displays the temperature measured at the center of the exposed area. As can be seen, the temperature profile of the bilayer nanocomposite in water can be readily adjusted by NIR pulsing.

Water will be secreted out during deswelling when the substrate is heated above its LCST under NIR irradiation. As a result, more FWCNT-doped PNIPAM will be pulled into the area that is under laser illumination. This leads to faster heating and a higher temperature rise. In the absence of NIPAM in the precursor that forms the top layer, there is only a small amount of shrinkage above the LCST and consequently even less PNIPAM will be exposed to the NIR irradiation and thus be heated. This results in a factor of 3 reduction in temperature rise in response to NIR exposure, as can be seen in Figure 4b_2. Nevertheless, if there is too much PNIPAM and not enough PAA in the top layer, cells will not adhere well due to insufficient collagen for adequate cell adhesion and large and abrupt shrinkage upon cooling below the LCST as demonstrated in Figure 4a in the case of AA:NIPAM = 1:2. We have found the optimized formulation is a 150-μm-thick top layer prepared from a monomer solution with the molar ratio of AA:NIPAM = 1:1. In order to have force effectively transmitted from the bottom layer to the top surface and then onto the cells, it is important that the entire nanocomposite can mechanically deform in response to NIR as one, as depicted in Figure 3b_2.

LCST, Surface Modulus, and Visualization of Dynamic NIR Response with Polystyrene Beads. The effect of an additional top layer and collagen grafting on the LCST was studied by measuring the change of optical transmission as a function of temperature as shown in Figure 5a. The LCST was estimated from the cloud point data and was defined as the temperature that exhibits a 50% change in transmittance.[45] Since the top layer is interpenetrated into the bottom layer, as expected, the presence of hydrophilic PAA shifts the LCST to higher temperature from 33 °C to 35 °C, which is more physiologically relevant. The collagen grafting has little impact on the LCST.

The net change in surface modulus controls the amount of strain and mechanical force that can be generated. Surface moduli were obtained from the ball indentation data on wetted substrates below and above the LCST. The force–displacement curves from measuring the contact force required to cause the indentation (displacement)[46] are shown in Figure S6. The surface moduli displayed in Figure 5b were estimated after the corrections to address the overestimation of the modulus from the Hertz contact model when applied to thin samples and the consideration that samples are bound to a rigid substrate (*i.e.*, glass coverslip).[47,48] Owing to covalent linkages and uniform distribution, as little as 0.02 wt % FWCNTs in the mechanoresponsive bottom layer can lead to almost 3 times enhancement of the elastic modulus, *i.e.*, from 36 kPa to 100 kPa at 25 °C and from 164 kPa to 406 kPa at 37 °C. There is a marginal reduction of surface stiffness after adding the thin top layer and grafting collagen. Nevertheless, these surfaces are much softer than conventional polystyrene Petri dish (5.4 GPa from the same measurement technique) for stem cell culture and differentiation. Table S1 tabulates the elastic modulus of each substrate below and above the LCST.

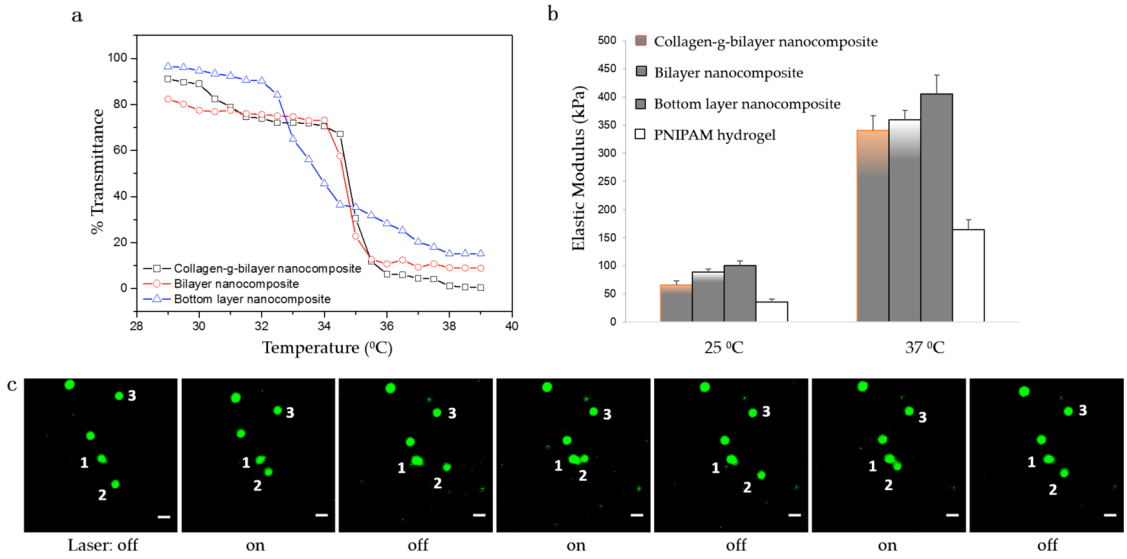

Figure 5. (a) Transmittance *vs* temperature. (b) Surface moduli using indentation with a ball radius of 1.5 mm and indentation depth of 90 μm. The standard deviation is calculated from five different samples for each substrate. (c) Fluorescent bead spatial distribution under NIR pulsing (980 nm, 200 mW, 0.05 Hz). Beads are labeled for clarity. Scale bars: 20 μm.

We employed green fluorescent polystyrene latex beads with a diameter of 10 μm to determine if NIR pulsing can induce spatial- and temporal-specific force. It is known that cells will generate traction force in response to stiffness change and strain,[49−51] leading to complexity in the evaluation of the dynamic NIR response of a substrate. Beads can move passively under a force field. Figure 5c contains a set of fluorescence images showing the relative bead position with the laser on and off. Beads can be moved apart and back reversibly under a pulsed NIR of 0.05 Hz. At the heating center, the strain can reach 60% within 10 s, indicated by the point-to-point distance between bead 1 and 2 with ImageJ (version 1.48). The displacement between bead 2 and 3 in the peripheral region is observed to be 30%, whereas the overall constriction (*i.e.*, elastic deformation of the image, as defined by the ImageJ plugin bUwarpJ)[52] in the field of view is only 10%. The analysis images are shown in the Supporting Information, Figure S8. This result confirms that spatiotemporal force can be generated reproducibly using the nanocomposite substrate in conjunction with NIR. To the best of our knowledge, this is the first demonstration of a material platform enabled by nanotechnology that can generate spatially controlled force sequences.

Beam Spreading and Intensity Attenuation from Theory and Experiments. Since NIR was used to induce strain/deformation produced by deswelling PNIPAM in an aqueous media, the effect of water on heat transfer and beam spread was investigated. A thermal influx with a beam diameter of 3 mm and a power of 200 mW was used to emulate the optothermal effect of a NIR laser. Figure 6a is a COMSOL (version 4.3) simulation result comparing temperature profiles of a dry (in air) *vs* hydrated (in water) substrate (porous PNIPAM matrix, thermal conductivity 0.025 W/(m·K), heat capacity 1395 J/(kg·K), density 1100 kg/m^3) under NIR irradiation.

When the dry substrate is placed in air, within a 15 s irradiation, the temperature of the bottom will rise to 41 °C. The top surface can also reach 41 °C. The beam spot size will remain more or less the same. On the other hand, when the same substrate is immersed in water, due to higher thermal conductivity of water (0.6 W/(m·K) (water) vs 0.025 W/(m·K) (air)), the temperature of the bottom will rise to 40 °C after a 15 s irradiation, and the effective beam size was 1.5 times greater than the original spot size. The highest temperature that the top surface can reach is about 36 °C.

In addition to the thermal-related intensity loss, various optical factors such as scattering and refraction can further attenuate the intensity and thus lower the temperature rise, and also diffuse the beam. We chose a 1.5-mm-thick bottom layer, the minimum thickness to provide sufficient deformation. Figure 6b$_1$ contains the temperature profiles of the top surface of our current bilayer nanocomposite substrate in air and in water. After 15 s, the central temperature at the surface of the substrate in air can reach 42 °C, whereas the central temperature at the surface of the substrate in water is about 37 °C. Since the aforementioned simulation did not consider the optical effect, one would expect that the experimental data that include both thermal and optical factors should show noticeably less temperature rise. On the contrary, the experimental temperature rise (37 °C) is slightly higher than what the simulation predicts (36 °C), suggesting that the optothermal effect generated by CNTs is more effective than conventional thermal influx.

Figure 6b$_2$ contains the radial temperature profile of the substrate surface and the corresponding

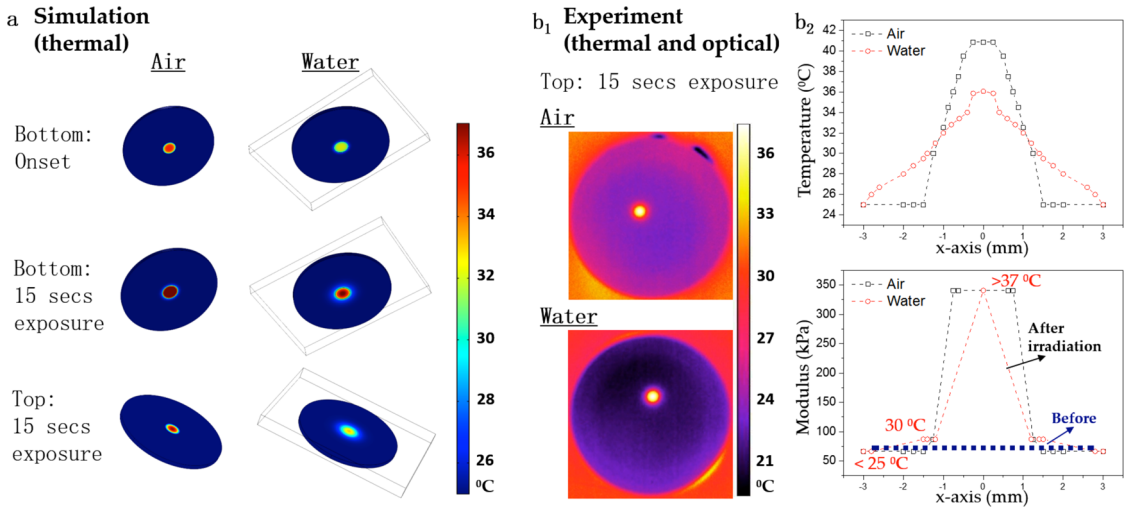

Figure 6. Temperature profile of the bilayer nanocomposite. (a) Modeling results of the effect of water on beam dispersion and heat loss. (b) Experimental results of heat loss and the beam dispersion and calculated modulus profile of the bilayer nanocomposite's top surface.

modulus profile calculated from the experimental elastic moduli data. Due to a nonlinear response, the area generated by strain is smaller than, if not similar to, the NIR exposed area. Since state-of-the-art optical tools can readily produce the beam diameter of a laser in the submicrometer region, it is expected that subcellular force can be applied to cells for polarization as an example.

Cell Shape Changes in Response to NIR Actuation. While a great deal of research has been focused on the influences of shear flow and surface stiffness on cell behavior, few approaches have been developed to engineer spatially and temporally controlled forces that can mimic the *in situ* environment to which cells are exposed. Using NIR stimulation of the bilayer nanocomposite substrate creates engineered forces with spatiotemporal control. Figure 7 contains representative fluorescence images demonstrating that cell shape is expanded and contracted in sync with NIR-induced nanocomposite swelling and deswelling. Thermal energy induced by NIR irradiation will heat the bottom layer nanocomposite above the LCST and thus cause shrinkage around the laser-exposed area. The generated compression force can be transmitted onto cells and lead to cell shape changes. Consistently, an average of 50% lateral shrinkage in the image sets (Figure 7) is obtained at the center of irradiation, while in the adjacent area roughly 30% shrinkage is observed. (The analysis details can be found in Figure S9.) Cells were still alive after extended NIR actuation, implying that both the substrate and the NIR influx do not cause significant cell apoptosis throughout the culturing and actuation process.

A platform that can exert programmed time- and space-dependent mechanical forces is highly desirable for a fundamental investigation of mechanical cues on phenotypic development and regulation of cell function. For example, it has been hypothesized that low

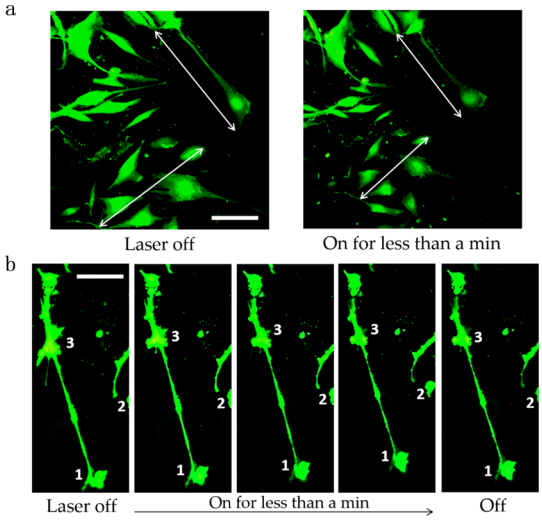

Figure 7. Fluorescence images of calcein AM-stained hTERT-FHs on the bilayer nanocomposite substrate upon laser illumination (980 nm, 200 mW) for 1 min. Scale bars: 100 μm.

shear force coupled with continuous perfusion, mimicking the native hemodynamics, can promote the maintenance of liver function *in vitro*.[53] In the current experiment, a single "point" laser was employed to apply localized stimulation. A spatial light modulator allows the formation of time-specific force patterns that are otherwise difficult to create. This platform, which can generate localized heating and impose spatiotemporal forces, offers at least four distinct advantages over the electrical resistive heating approach. First is the ability to induce localized heating from nanoscale domains without involving complicated fabrication of a pixelated heating pad array required for electrical heating. Second is fast heating and cooling due to uniform distribution of highly thermally conductive CNTs. Third is nanoheaters being covalently bound with the polymeric hydrogel so that they can act as

one to produce a large and reversible mechanoresponse under NIR stimulation. Fourth, the effective heating spots can be obtained with a much higher resolution (*i.e.*, with evenly distributed nanotubes) than that of a pixelated heating pad (typically 150 by 150 μm). The creation of this platform thus paves a pathway to recapitulate the dynamic cellular environment to study cell differentiation. This NIR mechanoresponsive nanocomposite can be exploited for different biomedical applications such as drug delivery, biopumps, and biovalves, all of which will benefit from remote/versatile NIR actuation.

CONCLUSIONS

We have designed macromonomer-grafted FWCNTs for uniform dispersion of FWCNTs and for the formation of covalent linkages between FWCNTs and a thermoresponsive PNIPAM matrix. Only 0.02 wt % FWCNTs is needed to reinforce the polymeric hydrogel, *e.g.*, a 36 kPa (pure hydrogel) to 100 kPa (0.02 wt % FWCNT loading at 25 °C) improvement in elastic modulus, and to generate an appreciable and reversible mechanoresponse. We have fabricated the bilayer nanocomposite substrate by incorporating a cell-seeding layer that interpenetrates into the bottom layer with the top surface functionalized with collagens. We have demonstrated that mechanical deformation can be generated reproducibly by monitoring the motion of fluorescent polystyrene beads under NIR pulsing. More significantly, we have demonstrated that cell shapes can be altered with no apoptosis and that cells remain attached to this substrate during extended cyclic mechanical deformation. To the best of our knowledge, this is the first demonstration of a nanomaterial platform that can generate engineered physical forces with high spatial resolution with remote NIR stimuli.

METHODS

Synthesis of MacroAA-*g*-FWCNTs. FWCNTs were kindly provided by J. Liu (Duke University). To purify and render surfaces more hydrophilic, FWCNTs were put into 5 M HNO_3 and sonicated for 30 min, followed by rinsing with deionized water. Samples were isolated using a 0.22 μm filter paper (PVDF Durapore Membrane Filter, Millipore) and subsequently vacuum-dried. Acrylic acid (AA, Sigma-Aldrich) was purified by distillation prior to use. The synthetic approach for macroAA-*g*-FWCNTs was adapted from our previously published method for PAA-*g*-CNTs.[41] Briefly, purified FWCNTs were mixed well with purified acrylic acid and acetone. Cysteamine (Sigma), an aminomercaptan chain transfer agent, and azobis(isobutyronitrile) (AIBN, Sigma-Aldrich) were then added to perform the precipitation polymerization at 70 °C under N_2 overnight. To further modify the polymer chain with a terminal methacrylamidyl group, the product was redispersed in tetrahydrofuran (THF, Sigma-Aldrich) and reacted for 2 h with methacryloyl chloride (Fluka Analytical) and triethylamine (Sigma-Aldrich). MacroAA-*g*-FWCNTs were filtrated, rinsed with THF followed by deionized water, and then vacuum-dried.

Characterizations of MacroAA-*g*-FWCNTs. ^{1}H NMR analysis was performed on an Avance 500 spectrometer (500 MHz, Bruker) in $CDCl_3$; tetramethylsilane (^{1}H NMR) was used as the internal standard. Morphologies of macroAA-*g*-FWCNTs and FWCNTs were viewed under scanning electron microscopy (SEM) using a FEI XL30 (Philips) operating at 20 kV. Transmission electron microscopy (TEM) was also performed on macroAA-*g*-FWCNTs with a JEM-2010 FEF microscope (JEOL) working at 200 kV. Thermogravimetric analysis of the powder of macroAA-*g*-FWCNTs was carried out on an SDT Q600 system (TA Instruments) under N_2 flow at a ramping rate of 10 °C/min. Purified FWCNTs and PAA (MW 1800, Aldrich) were also tested.

Bottom Layer Formation. To fabricate the NIR mechanoresponsive bottom layer only, a glass coverslip was dabbed with 3-(trimethoxysilyl)propyl methacrylate (Aldrich) and baked at 90 °C for 30 min. The macroAA-*g*-FWCNT (0.025 wt %) suspension was blended into a precursor solution of NIPAM (Sigma-Aldrich), ethoxylated (20) trimethylolpropane triacrylate SR415 (Sartomer Co.), and *N*,*N*,*N*′,*N*′-tetramethylethylenediamine (Sigma-Aldrich). The concentration of NIPAM is 1.2 mol/L. After purging with N_2 for 30 min, the solution was poured into a Teflon mold with a flat silicon wafer placed on the bottom. Subsequently, ammonium persulfate (Sigma-Aldrich), the initiator, was added before placing the treated coverslip on the top. To generate patterns, a patterned Si wafer was used in the mold instead of the flat one. A series of patterns (150 μm square with the height of 10 μm) on the Si wafer were transferred onto the substrate surface *via* imprinting. To facilitate lifting after the substrate formation, both the flat and the patterned Si surfaces were coated with RainX to render them more hydrophobic. The PNIPAM hydrogel blended with FWCNTs and the pure PNIPAM hydrogel were also prepared using the same procedure.

Examination of Optothermal Effect of the Bottom Layer Nanocomposite. The patterned bottom layers fully swollen in PBS solution (pH 7.4) were subjected to NIR pulsing (980 nm, 200 mW) using a laser (LDC 210C, series 200, Thorlabs) at a frequency of 0.033 Hz, illuminating from the bottom surface (as shown in Figure 3a). The snapshots were taken by an Infinity X-32 digital camera (Lumenera Corporation), and area fluctuations were measured with the Infinity Analyze software (version 6.1.0) for the calculation of lateral shrinkage.

Bilayer Nanocomposite Fabrication. The top layer precursor solution was prepared by mixing purified AA with NIPAM, SR415, ammonium hydroxide (BDH Chemicals), and isopropyl alcohol (BDH Chemicals). The AA:NIPAM molar ratio in the precursor solution was 1:0 (the concentration of acrylic acid is 1.8 mol/L), 1:1, and 1:2, respectively. In a Teflon mold, the top layer precursor solution was evenly applied to the bottom, followed by adding APS. After 5 min, the bottom precursor solution mentioned above mixed with APS was placed onto the partially polymerized top layer. A treated coverslip was then gently applied. All the precursor solutions were degassed with N_2 prior to placing them into the mold. The bilayer nanocomposite consisting of a gray-colored bottom layer with a thin whitish surface was formed after 3 h. After rinsing, the bilayer nanocomposite was stored in PBS solution at room temperature.

Collagen Grafting onto the Top Surface of the Bilayer Nanocomposite. To graft collagen, the bilayer nanocomposite was first soaked for 2 h in a PBS solution of 1 mg/mL *N*-hydroxysuccinimide (Aldrich) and 10 mg/mL *N*-(3-(dimethylamino)propyl)-*N*′-ethylcarbodiimide hydrochloride (EDC, Sigma-Aldrich), in order to fully activate the carboxylic groups from PAA on the surface of the top layer. The nanocomposite was then transferred into a bovine collagen type I solution (PureCol 3.1 mg/mL, Advanced Biomatrix) and let sit overnight at room temperature. The collagen-grafted bilayer was sanitized in 70% ethanol for 30 min first and was then exposed to germicidal UV irradiation (UV−C 30 W, USHIO) in a biosafety cabinet (Labconco) for 30 min. The sterilized nanocomposite substrate was preserved in PBS solution at 37 °C in a CO_2 incubator (VWR) prior to use. The bilayer nanocomposite without EDC/NHS activation was also prepared and soaked in a collagen solution.

Determination of the LCST. Optical transmission as a function of temperature was measured using a UV−visible absorbance reader (SpectraMax M2e, Molecular Devices). Each substrate was immersed in PBS (pH 7.4) in a cuvette until equilibrium was reached. The temperature was increased in 0.5 °C increments, and the transmittance at 600 nm was recorded 5 min after the temperature had reached the designated temperature. The LCST was defined as the temperature that offers a 50% change in transmittance. The average LCST was calculated from three independent scans.

Surface Modulus Measurements. Swollen (25 °C) and deswollen (37 °C) substrates are tested in a custom-built ball-on-flat tribometer with the interface software written in LabVIEW (National Instruments) by A. Martini (University of California−Merced). A silicon nitride bead with a radius of 1.5 mm was used as the ball indenter. Each loading/unloading cycle was carried out within 10 s. A modified Hertz model was employed to obtain the surface modulus using contact force curves plotted against indentation depth. The fitting equations are as follows.

$$E = \psi E_{\mathrm{H}}$$

$$E_{\mathrm{H}} = \frac{3(1-\nu^2)F_{\mathrm{indenter}}}{4R^{1/2}\delta^{3/2}}$$

$$\psi = \frac{1+2.3\omega}{1+1.15\omega^{1/3}+\alpha\left(\frac{R}{h}\right)\omega+\beta\left(\frac{R}{h}\right)\omega^2}$$

where R is the radius of indenter, δ is the indentation depth, and h and ν are the thickness and Poisson's ratio of the substrate, respectively. A correction factor ψ was applied to adjust the Hertz modulus (E_{H}).[48]

Cyclic Temperature Profiles of Bilayer Nanocomposites. The surface temperature of a bilayer nanocomposite substrate with different top layer prepared from the AA:NIPAM molar ratio of 1:0, 1:1, and 1:2 was monitored by an IR camera (SC600, FLIR Systems) during NIR pulsing (980 nm, 200 mW, 0.033 Hz). The change of temperature at the center of the laser exposure was recorded.

NIR Actuation of Fluorescent Beads. Green fluorescent polystyrene latex beads with a diameter of 10 μm (Magsphere Inc.) were added into the top layer precursor solution before polymerization. The bilayer nanocomposite in PBS solution was subjected to NIR pulsing (980 nm, 200 mW, 0.05 Hz) at 30 °C. Images of bead movement due to the lateral shrinkage of PNIPAM above the LCST were captured using a confocal laser scanning microscope system (Eclipse Ti, Nikon).

Investigation on Heat Transfer by Simulation. A porous PNIPAM matrix (thermal conductivity 0.025 W/(m·K), heat capacity 1395 J/(kg·K), density 1100 kg/m^3) was built with COMSOL (version 4.3, COMSOL Inc.) to visualize the heat transfer process for both dry and hydrated conditions by finite element analysis. A 3-mm-diameter thermal influx (200 mW) was confined at the bottom for 15 s. Both size and dose are identical to the laser power used in the experiment. The surface temperature contour was then constructed accordingly. The strain profile was demonstrated using the surface modulus as a function of temperature, as shown in Figure S7.

Cell Seeding and Actuation. Human telomerase reverse transcriptase-reconstituted human fetal hepatocytes from M. Zern (University of California−Davis) were seeded on the top of sterilized nanocomposite substrates and then incubated at 37 °C in 5% CO_2 for 3 days. The culture medium composed of Dulbecco's modified Eagle's medium (DMEM, Invitrogen) containing 10% fetal bovine serum (FBS, Invitrogen), 2.4 μg/mL hydrocortisone (Sigma), 5 μg/mL insulin (Sigma), 50 units/mL penicillin, and 50 μg/mL streptomycin (Invitrogen)[54] was refreshed on a daily basis. On the fourth day, cells were stained with cell viability dyes, comprising 2 μmol/L calcein AM and 4 μmol/L EthD-1 (Invitrogen), at 37 °C for 30 min. Nanocomposite substrates were then washed with PBS before subjected to NIR irradiation (980 nm, 200 mW) at 30 °C. Cell images were acquired using a Nikon Eclipse Ti confocal microscope. Cell morphology change was calculated with ImageJ (version 1.48, NIH).

Conflict of Interest: The authors declare no competing financial interest.

Acknowledgment. This work was supported by the National Science Foundation (NSF-Biomaterials 1309673) and the Muscular Dystrophy Association (MDA 154888). We thank C. Wang (Fudan University) for assistance with the NMR analysis, and J. Sharping and K. Andersen for help with the laser setup. We are also grateful to J. Liu (Duke University) for providing the carbon nanotubes, to A. Martini for granting access to the tribometer, and to M. Zern (University of California-Davis) for providing the cell line. Special thanks go to C. Viney for help with the IR camera and insightful comments on mechanical properties of the material.

Supporting Information Available: Optical images of nanocomposites prepared by macroAA-*g*-FWCNTs *vs* pure FWCNTs, lateral shrinkage of the nanocomposite upon 0.01 Hz NIR pulsing, transmission data as a function of temperature, fluorescence images of hTERT-FHs on different substrates, surface temperature profile of the nanocomposite, raw ball indentation data and corresponding calculated elastic modulus, table of LCSTs and elastic moduli, elastic modulus as a function of temperature, and detailed analyses of bead movement and cell shrinkage induced by NIR pulsing. This material is available free of charge *via* the Internet at http://pubs.acs.org.

REFERENCES AND NOTES

1. Guilak, F.; Cohen, D. M.; Estes, B. T.; Gimble, J. M.; Liedtke, W.; Chen, C. S. Control of Stem Cell Fate by Physical Interactions with the Extracellular Matrix. *Cell Stem Cell* **2009**, *5*, 17–26.
2. Wozniak, M. A.; Chen, C. S. Mechanotransduction in Development: A Growing Role for Contractility. *Nat. Rev. Mol. Cell Biol.* **2009**, *10*, 34–43.
3. Mammoto, T.; Ingber, D. E. Mechanical Control of Tissue and Organ. *Development* **2010**, *137*, 1407–1420.
4. Kilian, K. A.; Bugarija, B.; Lahn, B. T.; Mrksich, M. Geometric Cues for Directing the Differentiation of Mesenchymal Stem Cells. *Proc. Natl. Acad. Sci. U.S.A.* **2010**, *107*, 4872–4877.
5. Hoffman, B. D.; Grashoff, C.; Schwartz, M. A. Dynamic Molecular Processes Mediate Cellular Mechanotransduction. *Nature* **2011**, *475*, 316–323.
6. Li, D.; Zhou, J.; Chowdhury, F.; Cheng, J.; Wang, N.; Wang, F. Role of Mechanical Factors in Fate Decisions of Stem Cells. *Regener. Med.* **2011**, *6*, 229–240.
7. Lucitti, J. L.; Jones, E. A. V.; Huang, C.; Chen, J.; Fraser, S. E.; Dickinson, M. E. Vascular Remodeling of the Mouse Yolk Sac Requires Hemodynamic Force. *Development* **2007**, *134*, 3317–3326.
8. Freytes, D. O.; Wan, L. Q.; Vunjak-Novakovic, G. Geometry and Force Control of Cell Function. *J. Cell Biochem.* **2009**, *108*, 1047–1058.
9. Zimmermann, W.-H.; Schneiderbanger, K.; Schubert, P.; Didié, M.; Münzel, F.; Heubach, J. F.; Kostin, S.; Neuhuber, W. L.; Eschenhagen, T. Tissue Engineering of a Differentiated Cardiac Muscle Construct. *Cir. Res.* **2002**, *90*, 223–230.
10. Adamo, L.; Naveiras, O.; Wenzel, P. L.; McKinney-Freeman, S.; Mack, P. J.; Gracia-Sancho, J.; Suchy-Dicey, A.; Yoshimoto, M.; Lensch, M. W.; Yoder, M. C.; *et al*. Biomechanical Forces Promote Embryonic Haematopoiesis. *Nature* **2009**, *459*, 1131–1135.
11. Grayson, W. L.; Fröhlich, M.; Yeager, K.; Bhumiratana, S.; Chan, M. E.; Cannizzaro, C.; Wan, L. Q.; Liu, X. S.; Guo, X. E.; Vunjak-Novakovic, G. Engineering Anatomically Shaped Human Bone Grafts. *Proc. Natl. Acad. Sci. U.S.A.* **2010**, *107*, 3299–3304.
12. Huh, D.; Matthews, B. D.; Mammoto, A.; Montoya-Zavala, M.; Hsin, H. Y.; Ingber, D. E. Reconstituting Organ-Level Lung Functions on a Chip. *Science* **2010**, *328*, 1662–1668.
13. Akbari, S.; Shea, H. R. Microfabrication and Characterization of an Array of Dielectric Elastomer Actuators Generating

Uniaxial Strain to Stretch Individual Cells. *J. Micromech. Microeng.* **2012**, *22*, 045020.
14. Poh, Y.-C.; Shevtsov, S. P.; Chowdhury, F.; Wu, D. C.; Na, S.; Dundr, M.; Wang, N. Dynamic Force-Induced Direct Dissociation of Protein Complexes in a Nuclear Body in Living Cells. *Nat. Commun.* **2012**, *3*, 866.
15. DuFort, C. C.; Paszek, M. J.; Weaver, V. M. Balancing Forces: Architectural Control of Mechanotransduction. *Nat. Rev. Mol. Cell Biol.* **2011**, *12*, 308–319.
16. Poh, Y.-C.; Chen, J.; Hong, Y.; Yi, H.; Zhang, S.; Chen, J.; Wu, D. C.; Wang, L.; Jia, Q.; Singh, R.; *et al*. Generation of Organized Germ Layers from a Single Mouse Embryonic Stem Cell. *Nat. Commun.* **2014**, *5*, 4000.
17. Ebara, M.; Uto, K.; Idota, N.; Hoffman, J. M.; Aoyagi, T. Rewritable and Shape-Memory Soft Matter with Dynamically Tunable Microchannel Geometry in a Biological Temperature Range. *Soft Matter* **2013**, *9*, 3074–3080.
18. Schild, H. G. Poly(N-Isopropylacrylamide): Experiment, Theory and Application. *Prog. Polym. Sci.* **1992**, *17*, 163–249.
19. Kim, J.; Yoon, J.; Hayward, R. C. Dynamic Display of Biomolecular Patterns through an Elastic Creasing Instability of Stimuli-Responsive Hydrogels. *Nat. Mater.* **2009**, *9*, 159–164.
20. Yamaki, K.; Harada, I.; Goto, M.; Cho, C.-S.; Akaike, T. Regulation of Cellular Morphology Using Temperature-Responsive Hydrogel for Integrin-Mediated Mechanical Force Stimulation. *Biomaterials* **2009**, *30*, 1421–1427.
21. Yu, C.; Duan, Z.; Yuan, P.; Li, Y.; Su, Y.; Zhang, X.; Pan, Y.; Dai, L. L.; Nuzzo, R. G.; Huang, Y.; *et al*. Electronically Programmable, Reversible Shape Change in Two- and Three-Dimensional Hydrogel Structures. *Adv. Mater.* **2013**, *25*, 1541–1546.
22. Zhang, X.-Z.; Xu, X.-D.; Cheng, S.-X.; Zhuo, R.-X. Strategies to Improve the Response Rate of Thermosensitive PNIPAAm Hydrogels. *Soft Matter* **2008**, *4*, 385–391.
23. Liu, F.; Urban, M. W. Recent Advances and Challenges in Designing Stimuli-Responsive Polymers. *Prog. Polym. Sci.* **2010**, *35*, 3–23.
24. Sada, T.; Fujigaya, T.; Niidome, Y.; Nakazawa, K.; Nakashima, N. Near-IR Laser-Triggered Target Cell Collection Using a Carbon Nanotube-Based Cell-Cultured Substrate. *ACS Nano* **2011**, *5*, 4414–4421.
25. Kozai, T. D. Y.; Langhals, N. B.; Patel, P. R.; Deng, X.; Zhang, H.; Smith, K. L.; Lahann, J.; Kotov, N. A.; Kipke, D. R. Ultrasmall Implantable Composite Microelectrodes with Bioactive Surfaces for Chronic Neural Interfaces. *Nat. Mater.* **2012**, *11*, 1065–1073.
26. Zhang, H.; Patel, P. R.; Xie, Z.; Swanson, S. D.; Wang, X.; Kotov, N. A. Tissue-Compliant Neural Implants from Microfabricated Carbon Nanotube Multilayer Composite. *ACS Nano* **2013**, *7*, 7619–7629.
27. Shin, S. R.; Jung, S. M.; Zalabany, M.; Kim, K.; Zorlutuna, P.; Kim, S. bok; Nikkhah, M.; Khabiry, M.; Azize, M.; Kong, J.; *et al*. Carbon-Nanotube-Embedded Hydrogel Sheets for Engineering Cardiac Constructs and Bioactuators. *ACS Nano* **2013**, *7*, 2369–2380.
28. Kharaziha, M.; Shin, S. R.; Nikkhah, M.; Topkaya, S. N.; Masoumi, N.; Annabi, N.; Dokmeci, M. R.; Khademhosseini, A. Tough and Flexible CNT−Polymeric Hybrid Scaffolds for Engineering Cardiac Constructs. *Biomaterials* **2014**, *35*, 7346–7354.
29. Carey, B. J.; Patra, P. K.; Ci, L.; Silva, G. G.; Ajayan, P. M. Observation of Dynamic Strain Hardening in Polymer Nanocomposites. *ACS Nano* **2011**, *5*, 2715–2722.
30. Meaud, J.; Sain, T.; Yeom, B.; Park, S. J.; Shoultz, A. B.; Hulbert, G.; Ma, Z.-D.; Kotov, N. A.; Hart, A. J.; Arruda, E. M.; *et al*. Simultaneously High Stiffness and Damping in Nano-engineered Microtruss Composites. *ACS Nano* **2014**, *8*, 3468–3475.
31. Yang, L.; Setyowati, K.; Li, A.; Gong, S.; Chen, J. Reversible Infrared Actuation of Carbon Nanotube-Liquid Crystalline Elastomer Nanocomposites. *Adv. Mater.* **2008**, *20*, 2271–2275.
32. Pastine, S. J.; Okawa, D.; Zettl, A.; Fréchet, J. M. J. Chemicals on Demand with Phototriggerable Microcapsules. *J. Am. Chem. Soc.* **2009**, *131*, 13586–13587.
33. Du, R.; Wu, J.; Chen, L.; Huang, H.; Zhang, X.; Zhang, J. Hierarchical Hydrogen Bonds Directed Multi-Functional Carbon Nanotube-Based Supramolecular Hydrogels. *Small* **2014**, *10*, 1387–1393.
34. Kam, N. W. S.; O'Connell, M.; Wisdom, J. A.; Dai, H. Carbon Nanotubes as Multifunctional Biological Transporters and near-Infrared Agents for Selective Cancer Cell Destruction. *Proc. Natl. Acad. Sci. U.S.A.* **2005**, *102*, 11600–11605.
35. You, J.; Heo, J. S.; Kim, J.; Park, T.; Kim, B.; Kim, H.-S.; Choi, Y.; Kim, H. O.; Kim, E. Noninvasive Photodetachment of Stem Cells on Tunable Conductive Polymer Nano Thin Films: Selective Harvesting and Preserved Differentiation Capacity. *ACS Nano* **2013**, *7*, 4119–4128.
36. Wang, T.; Feng, Z.-Q.; Leach, M. K.; Wu, J.; Jiang, Q. Nanoporous Fibers of Type-I Collagen Coated Poly-(L-Lactic Acid) for Enhancing Primary Hepatocyte Growth and Function. *J. Mater. Chem. B* **2012**, *1*, 339–346.
37. Kung, J. W. C.; Currie, I. S.; Forbes, S. J.; Ross, J. A. Liver Development, Regeneration, and Carcinogenesis. *J. Biomed. Biotechnol.* **2010**, *2010*, 984248.
38. Hou, Y.; Tang, J.; Zhang, H.; Qian, C.; Feng, Y.; Liu, J. Functionalized Few-Walled Carbon Nanotubes for Mechanical Reinforcement of Polymeric Composites. *ACS Nano* **2009**, *3*, 1057–1062.
39. Ghosh, S.; Dutta, S.; Gomes, E.; Carroll, D.; D'Agostino, R.; Olson, J.; Guthold, M.; Gmeiner, W. H. Increased Heating Efficiency and Selective Thermal Ablation of Malignant Tissue with DNA-Encased Multiwalled Carbon Nanotubes. *ACS Nano* **2009**, *3*, 2667–2673.
40. Markovic, Z. M.; Harhaji-Trajkovic, L. M.; Todorovic-Markovic, B. M.; Kepić, D. P.; Arsikin, K. M.; Jovanović, S. P.; Pantovic, A. C.; Dramićanin, M. D.; Trajkovic, V. S. *In Vitro* Comparison of the Photothermal Anticancer Activity of Graphene Nanoparticles and Carbon Nanotubes. *Biomaterials* **2011**, *32*, 1121–1129.
41. Chao, T.-I.; Xiang, S.; Chen, C.-S.; Chin, W.-C.; Nelson, A. J.; Wang, C.; Lu, J. Carbon Nanotubes Promote Neuron Differentiation from Human Embryonic Stem Cells. *Biochem. Biophys. Res. Commun.* **2009**, *384*, 426–430.
42. Chao, T.-I.; Xiang, S.; Lipstate, J. F.; Wang, C.; Lu, J. Poly-(methacrylic Acid)-Grafted Carbon Nanotube Scaffolds Enhance Differentiation of hESCs into Neuronal Cells. *Adv. Mater.* **2010**, *22*, 3542–3547.
43. Tsuda, Y.; Kikuchi, A.; Yamato, M.; Nakao, A.; Sakurai, Y.; Umezu, M.; Okano, T. The Use of Patterned Dual Thermoresponsive Surfaces for the Collective Recovery as Co-Cultured Cell Sheets. *Biomaterials* **2005**, *26*, 1885–1893.
44. Chen, Y.-S.; Tsou, P.-C.; Lo, J.-M.; Tsai, H.-C.; Wang, Y.-Z.; Hsiue, G.-H. Poly(N-Isopropylacrylamide) Hydrogels with Interpenetrating Multiwalled Carbon Nanotubes for Cell Sheet Engineering. *Biomaterials* **2013**, *34*, 7328–7334.
45. Xia, Y.; Burke, N. A. D.; Stöver, H. D. H. End Group Effect on the Thermal Response of Narrow-Disperse Poly-(N-Isopropylacrylamide) Prepared by Atom Transfer Radical Polymerization. *Macromolecules* **2006**, *39*, 2275–2283.
46. Schmidt, S.; Zeiser, M.; Hellweg, T.; Duschl, C.; Fery, A.; Möhwald, H. Adhesion and Mechanical Properties of PNIPAM Microgel Films and Their Potential Use as Switchable Cell Culture Substrates. *Adv. Funct. Mater.* **2010**, *20*, 3235–3243.
47. Dimitriadis, E. K.; Horkay, F.; Maresca, J.; Kachar, B.; Chadwick, R. S. Determination of Elastic Moduli of Thin Layers of Soft Material Using the Atomic Force Microscope. *Biophys. J.* **2002**, *82*, 2798–2810.
48. Long, R.; Hall, M. S.; Wu, M.; Hui, C.-Y. Effects of Gel Thickness on Microscopic Indentation Measurements of Gel Modulus. *Biophys. J.* **2011**, *101*, 643–650.
49. Chen, C. S. Mechanotransduction−a Field Pulling Together? *J. Cell Sci.* **2008**, *121*, 3285–3292.
50. Vogel, V.; Sheetz, M. P. Cell Fate Regulation by Coupling Mechanical Cycles to Biochemical Signaling Pathways. *Curr. Opin. Cell Biol.* **2009**, *21*, 38–46.
51. Kim, I. L.; Khetan, S.; Baker, B. M.; Chen, C. S.; Burdick, J. A. Fibrous Hyaluronic Acid Hydrogels That Direct MSC

Chondrogenesis through Mechanical and Adhesive Cues. *Biomaterials* **2013**, *34*, 5571–5580.
52. Nishitani, W. S.; Saif, T. A.; Wang, Y. Calcium Signaling in Live Cells on Elastic Gels under Mechanical Vibration at Subcellular Levels. *PLoS One* **2011**, *6*, e26181.
53. Ebrahimkhani, M. R.; Neiman, J. A. S.; Raredon, M. S. B.; Hughes, D. J.; Griffith, L. G. Bioreactor Technologies to Support Liver Function *in Vitro*. *Adv. Drug Delivery Rev.* **2014**, *69–70*, 132–157.
54. Wege, H.; Le, H. T.; Chui, M. S.; Liu, L.; Wu, J.; Giri, R.; Malhi, H.; Sappal, B. S.; Kumaran, V.; Gupta, S.; *et al*. Telomerase Reconstitution Immortalizes Human Fetal Hepatocytes without Disrupting Their Differentiation Potential. *Gastroenterology* **2003**, *124*, 432–444.